

Superconductivity and band topology of double-layer honeycomb structure M_2N_2 (M = Nb, Ta)

Jin-Han Tan(谭锦函), Na Jiao(焦娜), Meng-Meng Zheng(郑萌萌), Ping Zhang(张平), and Hong-Yan Lu(路洪艳)
Citatio: Chin. Phys. B, 2025, 34 (**9**): 097402. DOI: 10.1088/1674-1056/adee04
http://cpb.iphy.ac.cn; http://iopscience.iop.org/cpb

What follows is a list of articles you may be interested in

Superconductivity in YbN_4H_{12} under low pressures

Xiang Wang(汪翔), Chenlong Xie(谢晨龙), Haohao Hong(洪浩豪), Yanliang Wei(魏衍亮), Zhao Liu(刘召), and Tian Cui(崔田)
Chin. Phys. B, 2025, 34 (**8**): 087401. DOI: 10.1088/1674-1056/add908

Realization of robust Ohmic contact for semiconducting black arsenic by coupling with graphene

Xinjuan Cheng(程新娟) and Xuechao Zhai(翟学超)
Chin. Phys. B, 2025, 34 (**2**): 027402. DOI: 10.1088/1674-1056/ada0b3

Phonon-mediated superconductivity in orthorhombic XS (X = Nb, Ta or W)

Guo-Hua Liu(刘国华), Kai-Yue Jiang(江恺悦), Yi Wan(万一), Shu-Xiang Qiao(乔树祥), Jin-Han Tan(谭锦函), Na Jiao(焦娜), Ping Zhang(张平), and Hong-Yan Lu(路洪艳)
Chin. Phys. B, 2025, 34 (**2**): 027401. DOI: 10.1088/1674-1056/ad9733

Experimental observation of Fermi-level flat band in novel kagome metal $CeNi_5$

Xue-Zhi Chen(陈学智), Le Wang(王乐), Shuai Zhang(张帅), Ren-Jie Zhang(张任杰), Yi-Wei Cheng(程以伟), Yu-Dong Hu(胡裕栋), Cheng-Nuo Meng(孟承诺), Zheng-Tai Liu(刘正太), Bai-Qing Lv(吕佰晴), and Yao-Bo Huang(黄耀波)
Chin. Phys. B, 2024, 33 (**8**): 087402. DOI: 10.1088/1674-1056/ad4019

Moiré superlattices arising from growth induced by screw dislocations in layered materials

Fuyu Tian(田伏钰), Muhammad Faizan, Xin He(贺欣), Yuanhui Sun(孙远慧), and Lijun Zhang(张立军)
Chin. Phys. B, 2024, 33 (**7**): 077403. DOI: 10.1088/1674-1056/ad4cdc

---

RAPID COMMUNICATION

Superconductivity and band topology of double-layer honeycomb structure M_2N_2 (M = Nb, Ta)

Jin-Han Tan(谭锦函)[1], Na Jiao(焦娜)[1], Meng-Meng Zheng(郑萌萌)[1,†], Ping Zhang(张平)[1,2], and Hong-Yan Lu(路洪艳)[1,‡]

[1] *School of Physics and Physical Engineering, Qufu Normal University, Qufu* 273165, *China*
[2] *Institute of Applied Physics and Computational Mathematics, Beijing* 100088, *China*

(Received 16 June 2025; revised manuscript received 7 July 2025; accepted manuscript online 10 July 2025)

Two-dimensional double-layer honeycomb (DLHC) materials are known for their diverse physical properties, but superconductivity has been a notably absent characteristic in this structure. We address this gap by investigating M_2N_2 (M = Nb, Ta) with DLHC structure using first-principles calculations. Our results show that M_2N_2 are stable and metallic, exhibiting superconducting behavior. Specifically, Nb_2N_2 and Ta_2N_2 display superconducting transition temperatures of 6.8 K and 8.8 K, respectively. Their electron–phonon coupling is predominantly driven by the coupling between metal d-orbitals and low-frequency metal-dominated vibration modes. Interestingly, two compounds also exhibit non-trivial band topology. Thus, M_2N_2 are promising platforms for studying the interplay between topology and superconductivity and fill the gap in superconductivity research for DLHC materials.

Keywords: first-principles calculations, phonon-mediated superconductivity, double-layer honeycomb structure, band topology

PACS: 74.20.Pq, 74.25.–q, 74.25.Jb, 74.78.–w

DOI: 10.1088/1674-1056/adee04 **CSTR:** 32038.14.CPB.adee04

1. Introduction

Two-dimensional (2D) materials have been extensively investigated across both experimental and theoretical domains for several decades. This is due to their unique physical characteristics, including exceptional optical properties and superconductivity,[1–4] and their significant potential for applications in nano-electronic devices and beyond.[5–7] Various types of 2D materials have been explored, such as graphene, which was successfully mechanically exfoliated in 2004,[8] and other materials including h-BN,[9–12] BCN, SiC, silicene,[13] germanene,[14] arsenene,[15] phosphorene,[16] tinene,[17] and transition metal dichalcogenides.[18–20] Researchers have employed methods like chemical vapor deposition and mechanical exfoliation to study these materials.[21,22] Some 2D materials, such as graphene[8] and silicene,[13] are derived from layered three-dimensional (3D) materials. However, certain 2D materials can form layered structures directly without originating from the bulk phase.[23] For example, double-layer honeycomb (DLHC) AlSb was synthesized on graphene-covered SiC substrates via molecular beam epitaxy (MBE) and has potential applications in sodium-ion and lithium-ion storage[24] and hybrid Hall-effect devices.[25] This structure differs from its 3D counterpart.[26]

As a significant member of the 2D family, honeycomb materials, including single-layer honeycomb (SLHC)[27–29] and DLHC structures,[30] have consistently been focal points of research. Unlike the single-layer six-membered ring of SLHC structure, the DLHC structure consists of two stacked six-membered rings. In the 2D limit, SLHC materials often exhibit insufficient stability, particularly for group III–V semiconductors. To address this challenge, the DLHC structure was proposed in 2018.[30] Since then, beyond AlSb, researchers have successfully synthesized other DLHC materials such as CuI and AgI, which can be stabilized under ambient conditions through direct growth within graphene packages.[31,32] DLHC has been predicted to exhibit semiconductor properties in III–V, II–VI, and I–VII compounds and shows diverse properties. For example, DLHC GaAs has been suggested as a platform for studying excitonic insulators.[31,33] Additionally, DLHC materials exhibit strong spin–orbit coupling (SOC), leading to topologically protected states like those in InSb, InAs, GaSb, GaAs, and HgTe,[30] making them promising for spintronics and quantum computing.[34,35] Their tunable electronic properties also make them suitable for transistors, energy storage, and nano-electronic devices,[36,37] while their strong van der Waals interactions suggest potential applications in flexible electronics.[38,39] For instance, Yi *et al.* proposed that AlP could serve as a potential anode material for alkali metal ion batteries.[40] Furthermore, DLHC materials like InN and AlAs possess excellent optical properties,

†Corresponding author. E-mail: qfzhmm@163.com
‡Corresponding author. E-mail: hylu@qfnu.edu.cn

© 2025 Chinese Physical Society and IOP Publishing Ltd. All rights, including for text and data mining, AI training, and similar technologies, are reserved.

including tunable band gaps, which present potential applications in photonics and optoelectronics.[41] However, superconductivity has been notably absent in DLHC structures, creating a significant gap in this field.

In this work, we perform first-principles calculations on the M_2N_2 (M = Nb, Ta) compounds with DLHC structure, consistent with experimentally realized materials such as AlSb,[26] to address the absence of superconductivity in DLHC structure. We identify two dynamically and thermodynamically stable superconductors: Nb_2N_2 and Ta_2N_2. The electronic structure, phonon spectrum, non-trivial band topology, electron–phonon coupling (EPC), and superconducting properties of these compounds are systematically investigated. From the calculated Eliashberg spectral function, the EPC constants (λ) are found to be 0.58 for Nb_2N_2 and 0.81 for Ta_2N_2, corresponding to superconducting transition temperatures (T_c) of 6.4 K and 8.8 K, respectively. These results represent a significant step forward in the search for superconductivity within DLHC systems. A detailed analysis reveals that in Nb_2N_2, superconductivity is primarily mediated by the interaction between Nb d-orbitals and low-frequency phonon modes. In Ta_2N_2, the EPC arises mainly from the coupling between Ta d-orbitals and low-frequency Ta-dominated vibrations. Additionally, both compounds exhibit non-trivial band topology. These findings provide new insight into the interplay between superconductivity and band topology in DLHC materials, offering a promising platform for future exploration of topological quantum phenomena.

2. Computational details

All the density functional theory (DFT)[42,43] calculations related to M_2N_2 structures in this study were conducted using the widely recognized Vienna *ab initio* simulation package (VASP)[44] and the Quantum Espresso (QE) package.[45] The interaction between electrons and ions was carried out by the projector augmented wave method (PAW).[46] For exchange–correlation effects, we employed the generalized gradient approximation (GGA) with the Perdew–Burke–Ernzerhof (PBE) functional.[47] The edge states were calculated using the iterative Green's function method implemented in the WANNIERTOOLS package,[48] based on a tight-binding model constructed from maximally localized Wannier functions generated by WANNIER90.[49,50] The Z_2 index was also computed using WANNIERTOOLS. In all calculations, the vacuum spacing was 20 Å along the c-axis was maintained to eliminate interactions between periodic images of the layers. For the electronic integration, we utilized a Γ-centered k-mesh of 18×18×1 for Brillouin zone sampling. For the phonon dispersion and EPC calculations, we used a q-point grid of 12×12×1 to sample the Brillouin zone, coupled with a high-resolution k-point grid of 48×48×1 to accurately compute the EPC matrix elements.

3. Results and discussion

3.1. Lattice structure and stability

The fully optimized DLHC structure of M_2N_2 exhibits hexagonal symmetry and belongs to the space group $P6/mmm$ (No. 191). Figure 1(a) presents the top and side views of this crystal structure, where green and gray spheres denote M and N atoms, respectively. Structurally, M_2N_2 adopts a DLHC configuration, consisting of two buckled M–N monolayers that are vertically stacked and interconnected via strong interlayer M–N bonds. In this arrangement, each M (N) atom in the bottom layer forms a single interlayer bond with one N (M) atom in the top layer, creating a compact and robust bilayer framework. The primitive unit cell contains four atoms, one M atom and one N atom in each layer, preserving the stoichiometry and symmetry of the DLHC prototype. Unlike the planar geometry of graphene, the six-membered rings in M_2N_2 display a consistent out-of-plane curvature, forming a bent bilayer structure with noticeable 3D character. This structural deformation is stabilized by the interlayer bonding and may significantly impact the electronic coupling and lattice dynamics. Table 1 summarizes the optimized structural parameters, including the in-plane lattice constant a, the intralayer bond length l, and the vertical interlayer distance h. Notably, Nb_2N_2 and Ta_2N_2 show nearly identical geometrical parameters, which can be attributed to their similar atomic radii and equivalent valence electron configurations, as both elements are group V transition metals. This structural similarity implies that the two

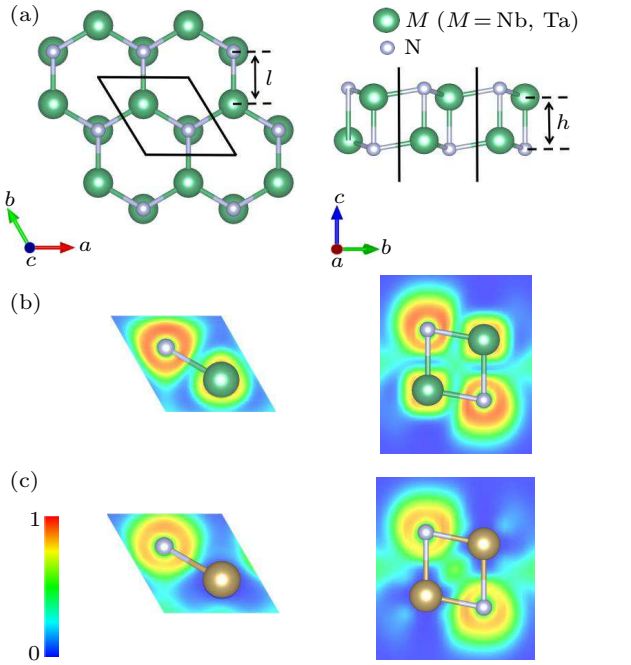


Fig. 1. (a) Top and side views of M_2N_2 (M = Nb, Ta). The unit cell is shown by the black solid line. M and N atoms are represented by green and gray spheres, respectively. The 2D maps of electron localization function for (b) Nb_2N_2 and (c) Ta_2N_2. The color of red and blue refer to the highest (1.0) and lowest (0.0) value of ELF, indicating accumulation and depletion of electrons, respectively.

compounds may exhibit analogous physical properties, including superconductivity. Additionally, we compared the a, l, and h of M_2N_2 with other DLHC compounds. The results indicate that the values for M_2N_2 fall within the normal range for DLHC materials.[26,30]

Table 1. Optimized lattice parameter a, bond lengths l and h, which are the distances between the M atom and the N atom in top view and side view.

	a (Å)	l (Å)	h (Å)
Nb_2N_2	3.52	2.07	2.23
Ta_2N_2	3.52	2.07	2.25

The stability of M_2N_2 is comprehensively evaluated from both thermodynamic and dynamical perspectives. For thermodynamic stability, *ab initio* molecular dynamics (AIMD) simulations at 300 K are carried out for both compounds. As illustrated in Figs. 2(a) and 2(b), the energies of Nb_2N_2 and Ta_2N_2 fluctuate around −675 eV and −632 eV, respectively, with no structural collapse or reconstruction observed during the simulations, indicating excellent thermal stability at room temperature. The cohesive energies (E_{coh}) and formation energies (E_{form}) are calculated to further assess thermodynamic stability. Using the formula $E_{coh} = [E_{M_2N_2} - (2E_M + 2E_N)]/4$, where $E_{M_2N_2}$ is the total energy of the optimized M_2N_2, and E_M and E_N are the total energies of isolated M (Nb or Ta) and N atoms, respectively, each calculated in large vacuum boxes to minimize spurious interactions due to periodic boundary conditions. The E_{coh} values obtained are −9.27 eV/atom for Nb_2N_2 and −9.11 eV/atom for Ta_2N_2. These values are significantly more negative than those of experimentally synthesized 2D materials, such as Cu_2Si (−3.46 eV/atom)[51,52] and DLHC AlSb (−5.04 eV/atom).[26,53] Additionally, compared to other DLHC nitrides like AlN (−5.65 eV/atom), GaN (−4.32 eV/atom), and InN (−3.73 eV/atom),[2] the more negative E_{coh} values for M_2N_2 not only imply superior structural cohesion but also suggest that M_2N_2 compounds may be more readily synthesizable under experimental conditions. The E_{form} is calculated using the relation $E_{form} = [E_{M_2N_2} - (2E_M + 2E_N)]/4$, the reference states are taken as body-centered cubic (BCC) phases for Nb and Ta, and N_2 molecules for N. The negative E_{form} (−4.03 eV/atom for Nb_2N_2 and −2.42 eV/atom for Ta_2N_2) further confirm the thermodynamic feasibility of synthesizing these compounds. Dynamical stability is assessed through phonon spectra, depicted in Figs. 4(a) and 4(f). The absence of imaginary phonon modes across the entire Brillouin zone confirms the dynamical stability of both Nb_2N_2 and Ta_2N_2. In summary, the combination of AIMD simulations, significantly negative E_{coh} and E_{form}, and positive phonon spectra provides compelling evidence for the thermodynamic and dynamical stability of M_2N_2. These findings underscore the structural viability of M_2N_2 and suggest their potential experimental accessibility. Techniques such as molecular beam epitaxy and chemical vapor deposition could potentially be used for their synthesis.

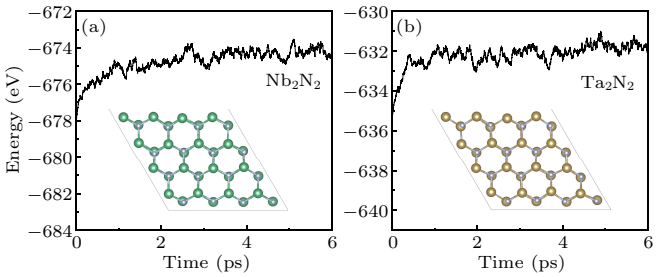


Fig. 2. The variation of the free energy in the AIMD simulations in the time scale of 6 ps along with the last frame of image at 300 K of (a) Nb_2N_2 and (b) Ta_2N_2, respectively.

3.2. Electronic structure and non-trivial band topology

Figure 3 illustrates the orbital-resolved electronic band structures, total density of states (DOS), and orbital-projected DOS (PDOS) for DLHC Nb_2N_2 and Ta_2N_2. The band structures along the high-symmetry path Γ–M–K–Γ are depicted in Figs. 3(a), 3(b) for Nb_2N_2, and in Figs. 3(f), 3(g) for Ta_2N_2. The corresponding Fermi surfaces (FSs), which reveal the nature of the low-energy electronic states, are shown in Figs. 3(e) and 3(j). Additionally, the electron localization function (ELF) plots in Figs. 1(b) and 1(c) provide insight into the spatial distribution of electron density within the unit cell.

Several energy bands intersect the Fermi level (E_F), confirming the metallic nature of both Nb_2N_2 and Ta_2N_2. In Nb_2N_2, three bands cross E_F, forming distinct Fermi pockets, one centered at the M point and another extending along the K–Γ direction, as shown in Fig. 3(e). The band with the highest Fermi velocity (v_F) lies along the Γ–K path, whereas the bands near the M point exhibit significantly lower v_F. The orbital-resolved band structures and PDOS [Fig. 3(d)] reveal that the low-energy electronic states near E_F are predominantly contributed by Nb d-orbitals. Among these, Nb d_{xz} and d_{yz} states dominate, followed by smaller contributions from Nb d_{z^2}, d_{xy}, and $d_{x^2-y^2}$. In contrast, the contribution from N atoms is minor, mainly arising from N p-orbitals. The electron localization function (ELF) in Fig. 1(b) further corroborates this picture, showing strong charge localization around N atoms. A similar metallic behavior is observed in Ta_2N_2, where three bands also cross E_F, as shown in Figs. 3(f) and 3(g). The corresponding FS [Fig. 3(j)] exhibits a prominent electron pocket around the Γ point and a hole pocket along the K–Γ direction. The highest v_F originates from the Γ–K band crossing. However, unlike Nb_2N_2, the v_F near the Γ point is comparatively lower. The PDOS [Fig. 3(i)] shows that Ta d-orbitals dominate the states near E_F, especially the Ta d_{xz} and d_{yz} components, followed by Ta d_{z^2} orbitals. A moderate contribution from Ta s-orbitals is also present, whereas the N-derived states are mainly from N s-orbitals, with minimal participation from N p-orbitals.

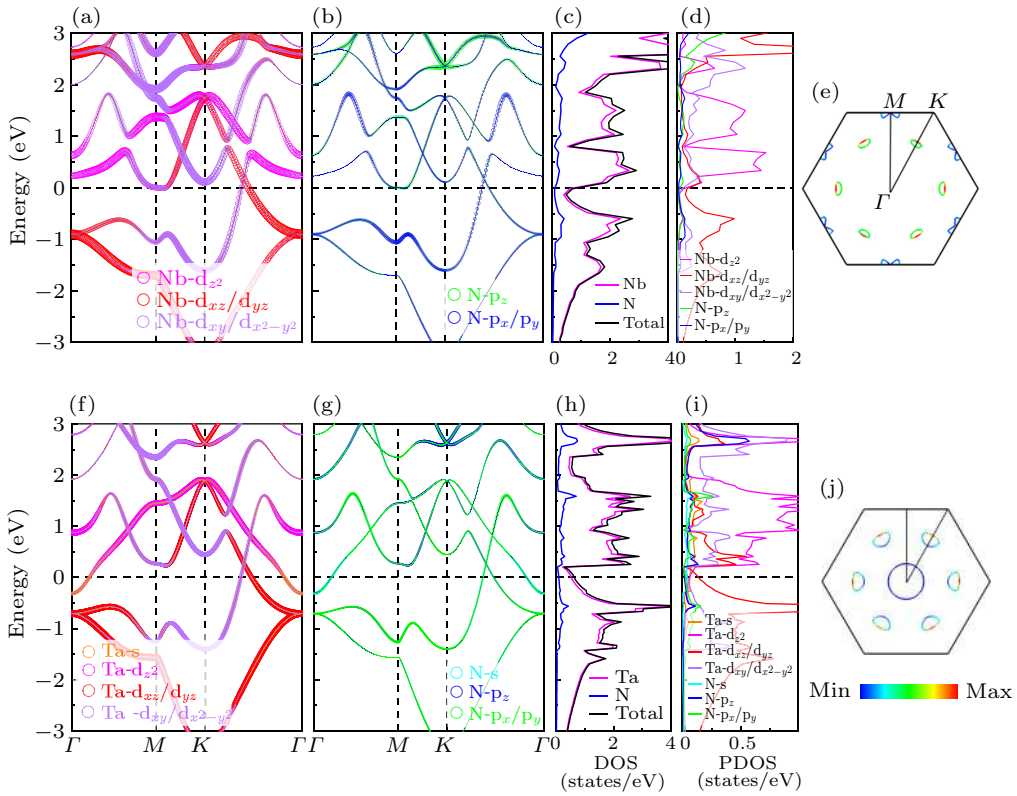


Fig. 3. Orbital-resolved electronic band structure along high-symmetry line of Γ–M–K–Γ for Nb (a) and N (b) of Nb_2N_2. (c) The total DOS of Nb_2N_2 and the total DOS of Nb and N atoms. (d) Orbital-projected DOS of Nb_2N_2. (f)–(i) are similar to (a)–(d) but for Ta_2N_2. FSs of (e) Nb_2N_2 and (j) Ta_2N_2. The high symmetric route along Γ–M–K–Γ is shown in black dotted lines.

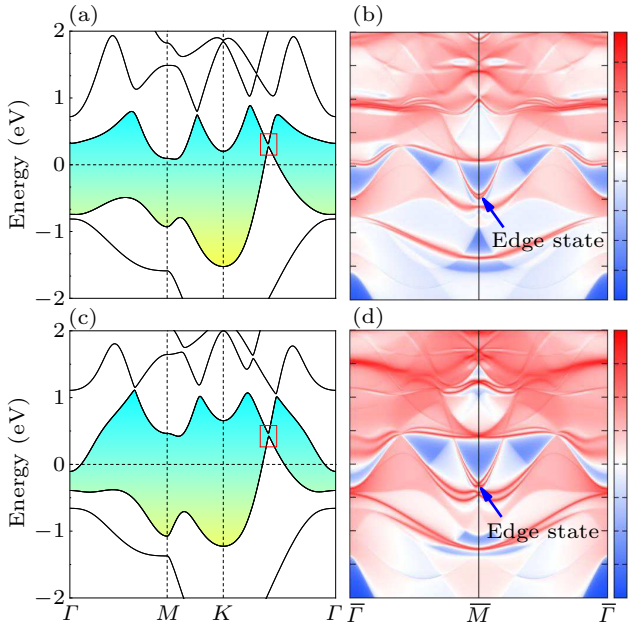


Fig. 4. The band structures with SOC and topological edge states (red trace) on the (0, 1) edge of (a), (b) Nb_2N_2 and (c), (d) Ta_2N_2.

To further elucidate the charge distribution and bonding characteristics, we performed Bader charge analysis. In Nb_2N_2, each Nb atom carries a Bader charge of approximately 3.47e, while each N atom holds about 6.53e. This indicates a net charge transfer of 1.53e from Nb to N. Similarly, in Ta_2N_2, the Ta atoms possess charges of 3.53e, and the N atoms have 6.47e, corresponding to a transfer of 1.47 electrons from Ta to N. This significant charge redistribution underscores the partially ionic character of the metal–N bonds. These results are consistent with the ELF maps [Figs. 1(b) and 1(c)] and the charge density difference (CDD) plot [Fig. S1], both of which show pronounced electron localization around the N atoms, reflecting their strong electronegativity and confirming the electron-donor role of the transition metal atoms. Furthermore, both the ELF and CDD reveal the presence of interstitial electronic states. In summary, the dominance of transition metal d-orbitals near the E_F underscores the pivotal role of metal–N bonding in determining the electronic structure of DLHC M_2N_2 compounds. Both ELF and Bader charge analyses highlight the significant electron-donating role of Nb. Furthermore, the pronounced d-orbital character near E_F creates favorable conditions for substantial EPC, which is a key factor in inducing superconductivity.

Moreover, both Nb_2N_2 and Ta_2N_2 exhibit Dirac-cone-like dispersions along the K–Γ path near the E_F. Upon inclusion of SOC, these Dirac points evolve into continuous band gaps, as highlighted in yellow in Figs. 4(a) and 4(c). The opening of SOC-induced gaps suggests a potential non-trivial topological character. To confirm this, we calculated the Z_2 topological index and obtained a value of 1 for both compounds, thereby confirming their non-trivial band topology. Additionally, as shown in Fig. S2, the Wannier charge centers (WCCs) cross the reference line an odd number of times, further supporting the topological nature of these materials. The existence of topologically protected edge states, evidenced by the red traces in Figs. 4(b) and 4(d), provides further validation of their non-

trivial topology. These results establish Nb_2N_2 and Ta_2N_2 as 2D topological metals with SOC-induced band gaps that can support robust edge states. Such properties make them highly promising for applications in spintronic devices and quantum information technologies.

3.3. Electron–phonon coupling and superconductivity

Given the metallic nature of Nb_2N_2 and Ta_2N_2 as indicated by their energy bands, it is crucial to further investigate their EPC and superconducting properties. Consequently, we calculate and analyze their phonon dispersion relations, phonon density of states (PhDOS), Eliashberg spectral function $\alpha^2F(\omega)$, cumulative EPC constant λ, and the integrated EPC distributions, with the results presented in Figs. 5 and 6.

For Nb_2N_2, the phonon modes can be categorized into three distinct frequency regions based on the phonon dispersion relations [Fig. 5(a)]: a high-frequency region ranging from 475 cm^{-1} to 610 cm^{-1}, a mid-frequency region from 375 cm^{-1} to 475 cm^{-1}, and a low-frequency region below 323 cm^{-1}. The high-frequency modes are predominantly attributed to in-plane vibrations of the lighter N atoms, while the mid-frequency modes mainly correspond to out-of-plane vibrations of the N atoms. As confirmed by the atom-resolved PhDOS in Fig. 5(c), the entire frequency range from 375 cm^{-1} to 610 cm^{-1} is almost entirely dominated by the vibration modes of N atoms. Below 323 cm^{-1}, the vibration modes become increasingly hybridized, involving both in-plane and out-of-plane displacements of Nb and N atoms. However, the dominant contributions in this low-frequency range are from Nb atoms, as evident in Fig. 5(c), where the phonon density of states (PhDOS) of Nb atoms dominates. The low-frequency region contributes approximately 70% of the total λ, as demonstrated by the Eliashberg spectral function $\alpha^2F(\omega)$ and the integrated EPC function λ in Fig. 5(d). This is consistent with Fig. 5(b), where the first acoustic branch shows strong EPC across most of the path except near the K point. Additionally, the EPC distribution in Fig. 5(b) matches that in Fig. 6(a). In summary, Nb plays a pivotal role in the superconductivity of Nb_2N_2. As evidenced by the electronic structure analysis, Nb provides nearly all the contributions at the Fermi level, especially from its d-orbitals. Therefore, the superconductivity in Nb_2N_2 primarily originates from the coupling between Nb d-orbitals electrons and mid- to low-frequency Nb vibrations. For Ta_2N_2, analogous phonon characteristics are observed. The vibration spectrum is divided into three regions: a high-frequency region (490–627 cm^{-1}), a mid-frequency region (340–478 cm^{-1}), and a low-frequency region below 220 cm^{-1}. Similar to the Nb analogue, the high- and mid-frequency modes are primarily associated with N atom vibrations, corresponding to in-plane and out-of-plane motions, respectively. In contrast, the low-frequency region involves more complex hybridized modes with contributions from both Ta and N atoms. The dominant phonon modes in this low-frequency range arise from the heavier Ta atoms, as illustrated in the atom-resolved PhDOS in Fig. 5(g). Significant EPC is concentrated in the first acoustic branch, particularly near point I along the K–Γ path, where pronounced phonon softening is observed, indicating a strong Kohn anomaly. The corresponding vibration pattern at point I is shown in the inset of Fig. 5(f), highlighting the enhanced EPC in this region. This corresponds to the orange-yellow arrow-shaped area near the K point along the K–Γ path in Fig. 6(b). As depicted in Fig. 5(h), over 80% of the EPC originates from the coupling of Ta d-orbitals [Fig. 3(i)] with low-frequency phonon modes below 220 cm^{-1}. This highlights the key role of Ta-derived vibrations in mediating the superconducting pairing mechanism. Based on the calculated EPC parameters and using the Allen-Dynes modified McMillan formula, the estimated T_c of Nb_2N_2 and Ta_2N_2 are 6.37 K and 8.80 K, respectively.

To further explore the tunability of superconductivity, strain engineering is applied to Nb_2N_2 and Ta_2N_2. The strain is applied along the two basis vector directions, and the relative change of the lattice constant ε is defined as $(a-a_0)/a_0 \times 100\%$, where a_0 and a represent the lattice constants of pristine and strained M_2N_2, respectively. For Nb_2N_2, applying a compressive strain of -1% primarily affects ω_{log}, reducing it from 311.27 K to 298.02 K, which lowers T_c to 6.08 K. In contrast, tensile strain induces dynamical instability, evidenced by imaginary frequencies in the phonon spectrum. For Ta_2N_2, a compressive strain of -2% decreases both λ and ω_{log}, lowering T_c to 5.23 K. Conversely, a tensile strain of 2% increases both λ and ω_{log}, raising T_c to 9.61 K. These findings indicate that compressive strain suppresses superconductivity in both materials, while tensile strain benefits superconductivity only in Ta_2N_2. All strained phonon spectra were confirmed to be free of imaginary modes, as shown in Fig. S3. The full details of the superconducting parameters for both the intrinsic and strained conditions are comprehensively listed in Table 2.

In addition to the phonon spectrum and EPC analyses, key superconducting parameters, such as the reduced energy gap $2\Delta(0)/k_BT_c$ and the isotope effect coefficient β, are evaluated to further elucidate the nature of superconductivity in these compounds. For Nb_2N_2, the calculated values are 3.59 and 0.44, respectively, while for Ta_2N_2, they are 3.76 and 0.47. The corresponding results are summarized in Table 3. These values are in close agreement with the predictions of conventional BCS theory, which estimates $2\Delta(0)/k_BT_c \approx 3.53$ and $\beta \approx 0.50$. The proximity of these values to the BCS limits strongly suggests that both Nb_2N_2 and Ta_2N_2 are conventional, phonon-mediated superconductors. Together with the EPC analysis, these findings provide a comprehensive theoretical foundation and valuable reference for the experimental exploration of superconductivity in these 2D DLHC materials.

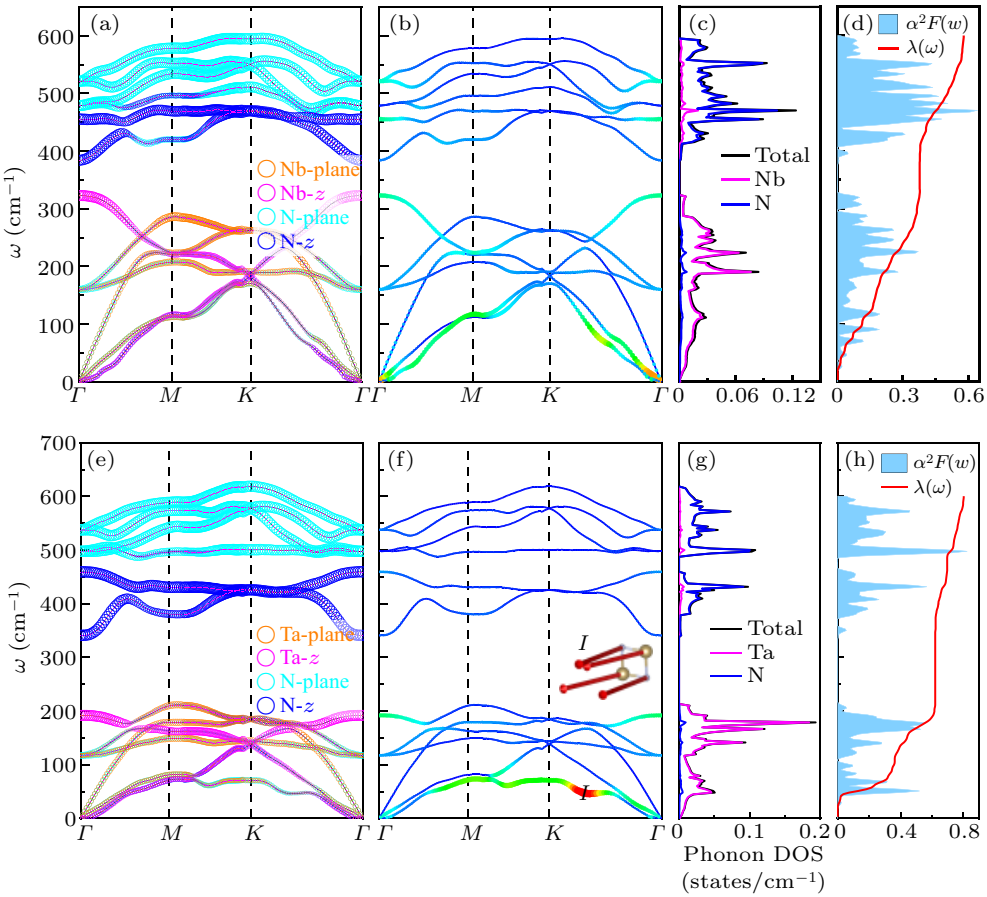


Fig. 5. Phonon dispersion of (a) Nb_2N_2 and (e) Ta_2N_2 weighted by the vibration modes of M and N atoms, respectively. (b), (f) Phonon dispersion weighted by the magnitude of EPC $\lambda_{q\nu}$. The insets show the vibration modes for the prominent $\lambda_{q\nu}$ I for Ta_2N_2. The brown and gray spheres represent Ta and N atoms, respectively. (c), (g) Total and atom-projected phonon DOS for Nb_2N_2 and Ta_2N_2. (d), (h) Eliashberg spectral function $\alpha^2F(\omega)$ and cumulative frequency dependence EPC function $\lambda(\omega)$ for Nb_2N_2 and Ta_2N_2.

Table 2. Biaxial strain ε, logarithmic averaged phonon frequency $\omega_{\log}$, total EPC constant λ, and superconducting T_c of M_2N_2.

	ε (%)	$\omega_{\log}$ (K)	λ	T_c (K)
Nb_2N_2	0	311.27	0.58	6.37
	–1	298.02	0.58	6.08
Ta_2N_2	0	185.10	0.81	8.80
	–2	131.11	0.74	5.23
	2	196.48	0.82	9.61

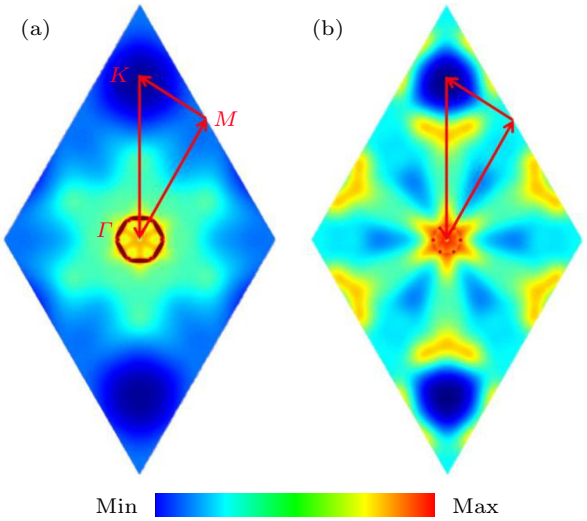


Fig. 6. The integrated EPC distributions of (a) Nb_2N_2 and (b) Ta_2N_2 in the plane of $q_z = 0$. The high-symmetry path of Γ–M–K–Γ is marked.

Table 3. The DOS at the Fermi level $N(E_F)$ (states/spin/Ry/unitcell), Sommerfeld constant γ (mJ/cm^3/K^2), specific heat jump at T_c $\Delta C(T_c)$ (mJ/cm^3/K^2), critical magnetic field at 0 K $H_c(0)$ (T), isotope coefficient β, and $2\Delta(0)/k_BT_c$ of Nb_2N_2 and Ta_2N_2.

	$N(E_F)$	γ	$\Delta C(T_c)$	$H_c(0)$	β	$2\Delta(0)/k_BT_c$
Nb_2N_2	12.70	0.03	0.05	0.03	0.44	3.59
Ta_2N_2	12.76	0.04	0.07	0.03	0.47	3.76

4. Conclusion

In summary, using first-principles calculations, we have systematically investigated M_2N_2 (M = Nb, Ta) with DLHC structure. We successfully identified Nb_2N_2 and Ta_2N_2 as the first DLHC materials exhibiting superconductivity, thereby addressing a key gap in this field. Both compounds display dynamically stable metallic behavior and significant EPC, with T_c of 6.37 K and 8.80 K, respectively. Their superconductivity primarily originates from d-orbitals of the transition metals (Nb and Ta) and low-frequency metal-dominated phonon modes. Notably, calculations of the Z_2 index and edge states reveal that Nb_2N_2 and Ta_2N_2 possess non-trivial band topology. The coexistence of superconductivity and non-trivial band topology not only enriches the understanding of DLHC systems but also provides a robust theoretical foundation and practical guidance for experimental research aimed at discov-

ering and designing DLHC compounds with combined superconducting and topological properties.

Acknowledgements

Project supported by the National Natural Science Foundation of China (Grant Nos. 12074213 and 11574108), the National Key R&D Program of China (Grant No. 2022YFA1403103), the Major Basic Program of Natural Science Foundation of Shandong Province (Grant No. ZR2021ZD01), the Natural Science Foundation of Shandong Province (Grant No. ZR2023MA082), and the Project of Introduction and Cultivation for Young Innovative Talents in Colleges and Universities of Shandong Province.

References

[1] Huang Z S, Zhang W X and Zhang W L 2016 *Materials* **9** 716
[2] Faraji M, Bafekry A, Fadlallah M M, Jappor H R, Nguyen C V and Ghergherehchi M 2022 *Appl. Surf. Sci* **590** 152998
[3] Muhsen Almayyali A O, Muhsen H O, Merdan M, Obeid M M and Jappor H R 2021 *Physica E* **126** 114487
[4] Yang L, Li Y P, Liu H D, Jiao N, Ni M Y, Lu H Y, Zhang P and Ting C S 2023 *Chin. Phys. Lett.* **40** 017402
[5] Xia F, Mueller T, Lin Y m, Valdes-Garcia A and Avouris P 2009 *Nat. Nanotechnol.* **4** 839
[6] Chen C, Mei W, Wang C, Yang Z, Chen X, Chen X and Liu T 2020 *J. Alloys Compd.* **826** 154122
[7] Bafekry A, Yagmurcukardes M, Akgenc B, Ghergherehchi M and Nguyen C V 2020 *J. Phys. D* **53** 355106
[8] Novoselov K S, Geim A K, Morozov S V, Jiang D, Zhang Y, Dubonos S V, Grigorieva I V and Firsov A A 2004 *Science* **306** 666
[9] Lin Y, Williams T V and Connell J W 2010 *J. Phys. Chem. Lett.* **1** 277
[10] Zhang K, Feng Y, Wang F, Yang Z and Wang J 2017 *J. Mater. Chem. C* **5** 11992
[11] Li L H and Chen Y 2016 *Adv. Funct. Mater.* **26** 2594
[12] Andrew R C, Mapasha R E, Ukpong A M and Chetty N 2012 *Phys. Rev. B* **85** 125428
[13] Vogt P, De Padova P, Quaresima C, Avila J, Frantzeskakis E, Asensio M C, Resta A, Ealet B and Le Lay G 2012 *Phys. Rev. Lett.* **108** 155501
[14] Derivaz M, Dentel D, Stephan R, Hanf M C, Mehdaoui A, Sonnet P and Pirri C 2015 *Nano Lett.* **15** 2510
[15] Kamal C and Ezawa M 2015 *Phys. Rev. B* **91** 085423
[16] Li L, Yu Y, Ye G J, Ge Q, Ou X, Wu H, Feng D, Chen X H and Zhang Y 2014 *Nat. Nanotechnol.* **9** 372
[17] Xu Y, Yan B, Zhang H J, Wang J, Xu G, Tang P, Duan W and Zhang S C 2013 *Phys. Rev. Lett.* **111** 136804
[18] Tan C, Qi X, Huang X, Yang J, Zheng B, An Z, Chen R, Wei J, Tang B Z, Huang W and Zhang H 2014 *Adv. Mater.* **26** 1735
[19] Komsa H P and Krasheninnikov A V 2012 *J. Phys. Chem. Lett.* **3** 3652
[20] Geng D and Yang H Y 2018 *Adv. Mater.* **30** 1800865
[21] Lei T, Liu C, Zhao J L, Li J M, Li Y P, Wang J O, Wu R, Qian H J, Wang H Q and Ibrahim K 2016 *J. Appl. Phys.* **119** 015302
[22] Liu H, Neal A T, Zhu Z, Luo Z, Xu X, Tománek D and Ye P D 2014 *ACS Nano* **8** 4033
[23] Molle A, Goldberger J, Houssa M, Xu Y, Zhang S C and Akinwande D 2017 *Nat. Mater.* **16** 163
[24] Son S Y, Lee D, Hur J and Kim I T 2017 *J. Nanosci. Nanotechnol.* **17** 7575
[25] Johnson M, Bennett B R, Yang M J, Miller M M and Shanabrook B V 1997 *Appl. Phys. Lett.* **71** 974
[26] Qin L, Zhang Z H, Jiang Z, Fan K, Zhang W H, Tang Q Y, Xia H N, Meng F, Zhang Q, Gu L, West D, Zhang S and Fu Y S 2021 *ACS Nano* **15** 8184
[27] Freeman C L, Claeyssens F, Allan N L and Harding J H 2006 *Phys. Rev. Lett.* **96** 066102
[28] Zhuang H L, Singh A K and Hennig R G 2013 *Phys. Rev. B* **87** 165415
[29] Zheng H, Li X B, Chen N K, Xie S Y, Tian W Q, Chen Y, Xia H, Zhang S B and Sun H B 2015 *Phys. Rev. B* **92** 115307
[30] Lucking M C, Xie W, Choe D H, West D, Lu T M and Zhang S B 2018 *Phys. Rev. Lett.* **120** 086101
[31] Mustonen K, Hofer C, Kotrusz P, Markevich A, Hulman M, Mangler C, Susi T, Pennycook T J, Hricovini K, Richter C, Meyer J C, Kotakoski J and Skákalová V 2022 *Adv. Mater.* **34** 2106922
[32] Andryushechkin B V and Pavlova T V 2022 *The Journal of Chemical Physics* **156** 164702
[33] Jiang Z, Li Y, Zhang S and Duan W 2018 *Phys. Rev. B* **98** 081408
[34] Liu C, Hughes T L, Qi X L, Wang K and Zhang S C 2008 *Phys. Rev. Lett.* **100** 236601
[35] Knez I, Du R R and Sullivan G 2011 *Phys. Rev. Lett.* **107** 136603
[36] Yi S, Liu G, Wan H, Liu Z, Hu W and Deng H 2021 *Appl. Surf. Sci.* **550** 149392
[37] Bafekry A, Faraji M, Fazeli S, H Khan S, Fadlallah M M, Stampfl C, Ghergherehchi M, Chang G S and Shokri B 2024 *J. Phys. Chem. C* **128** 8016
[38] Jiang H, Zheng L, Liu Z and Wang X 2020 *InfoMat* **2** 1077
[39] Duong D L, Yun S J and Lee Y H 2017 *ACS Nano* **11** 11803
[40] Yi S, Liu G, Liu Z, Hu W and Deng H 2020 *J. Phys. Chem. C* **124** 2978
[41] Bafekry A, Faraji M, Fadlallah M M, Jappor H R, Karbasizadeh S, Ghergherehchi M, Sarsari I A and Ziabari A A 2021 *Phys. Chem. Chem. Phys.* **23** 18752
[42] Hohenberg P and Kohn W 1964 *Phys. Rev.* **136** B864
[43] Kohn W and Sham L J 1965 *Phys. Rev.* **140** A1133
[44] Kresse G and Furthmüller J 1996 *Phys. Rev. B* **54** 11169
[45] Giannozzi P, Baroni S, Bonini N, Calandra M, Car R, Cavazzoni C, Ceresoli D, Chiarotti G L, Cococcioni M, Dabo I, Dal Corso A, de Gironcoli S, Fabris S, Fratesi G, Gebauer R, Gerstmann U, Gougoussis C, Kokalj A, Lazzeri M, Martin Samos L, Marzari N, Mauri F, Mazzarello R, Paolini S, Pasquarello A, Paulatto L, Sbraccia C, Scandolo S, Sclauzero G, Seitsonen A P, Smogunov A, Umari P and Wentzcovitch R M 2009 *J. Phys.: Condens. Matter* **21** 395502
[46] Kresse G and Joubert D 1999 *Phys. Rev. B* **59** 1758
[47] Perdew J P, Burke K and Ernzerhof M 1996 *Phys. Rev. Lett.* **77** 3865
[48] Wu Q, Zhang S, Song H F, Troyer M and Soluyanov A A 2018 *Comput. Phys. Commun.* **224** 405
[49] Pizzi G, Vitale V, Arita R, Blügel S, Freimuth F, Géranton G, Gibertini M, Gresch D, Johnson C, Koretsune T, Ibañez-Azpiroz J, Lee H, Lihm J M, Marchand D, Marrazzo A, Mokrousov Y, Mustafa J I, Nohara Y, Nomura Y, Paulatto L, Poncé S, Ponweiser T, Qiao J, Thöle F, Tsirkin S S, Wierzbowska M, Marzari N, Vanderbilt D, Souza I, Mostofi A A and Yates J R 2020 *J. Phys.: Condens. Matter* **32** 165902
[50] Marzari N, Mostofi A A, Yates J R, Souza I and Vanderbilt D 2012 *Rev. Mod. Phys.* **84** 1419
[51] Yang L M, Bačić V, Popov I A, Boldyrev A I, Heine T, Frauenheim T and Ganz E 2015 *J. Am. Chem. Soc.* **137** 2757
[52] Feng B, Fu B, Kasamatsu S, Ito S, Cheng P, Liu C C, Feng Y, Wu S, Mahatha S K, Sheverdyaeva P, Moras P, Arita M, Sugino O, Chiang T C, Shimada K, Miyamoto K, Okuda T, Wu K, Chen L, Yao Y and Matsuda I 2017 *Nat. Commun.* **8** 1007
[53] Bafekry A, Faraji M, Fadlallah M M, Jappor H R, Karbasizadeh S, Ghergherehchi M, Sarsari I A and Ziabari A A 2021 *Phys. Chem. Chem. Phys.* **23** 18752